Electric fields and stationary drift flows in the island divertor SOL of Wendelstein 7-X

Carsten Killer,[1] Dario Cipciar,[1] Seung Gyou Baek,[2] Sean B. Ballinger,[2]
Adrian von Stechow,[1] James L. Terry,[2] Olaf Grulke,[1,3] and W7-X Team*

[1] *Max-Planck-Institut für Plasmaphysik, Wendelsteinstr. 1, 17491 Greifswald, Deutschland*
[2] *Massachusetts Institute of Technology - Plasma Science and Fusion Center, Cambridge, MA 02139, USA*
[3] *Department of Physics, Technical University of Denmark, Lyngby, Denmark*

In the island divertor scrape-off layer (SOL) of the Wendelstein 7-X stellarator, 2D-resolved Langmuir probe measurements uncover a complex spatial structure of electron temperature, density, and floating potential. Depending on details of magnetic island size and position, significant poloidal gradients and non-monotonic radial profiles are observed. The resulting electric fields imply the presence of sheared stationary drift flows with poloidal velocities of a few km/s, with flow channels as narrow as one cm. Such flows are observed with a gas puff imaging diagnostic in qualitative agreement with the probe results and imply a significant transport channel in the SOL. The 2D distribution of plasma parameters is intricately associated with the unique magnetic structure of the island divertor SOL and highlights the necessity for more accurate magnetic field reconstructions.

I. INTRODUCTION

In the boundary of magnetic fusion plasmas, different energy and particle transport effects contribute to the equilibrium plasma profiles [1]: Parallel transport along open magnetic field lines is subject to sheath physics and parallel gradients, and has convective and conductive contributions. Cross-field transport in the form of convective drifts can occur in both radial (normal) and poloidal (bi-normal) direction, depending on the drift type. Finally, diffusive cross-field transport is often used to describe turbulent transport for mean-field transport models. (However, particularly in tokamaks, this assumption is disputed [2–4]).

In the non-axisymmetric geometry of stellarators, the assessment of these transport channels is complicated by the complex magnetic structure. Wendelstein 7-X uses an island divertor configuration, where the scrape-off layer (SOL) is formed by a chain of resonant magnetic islands that surround the main confined plasma and separate it from the divertor region [5–7], see Fig. 1.

Compared to the well-known divertors of tokamaks, the island divertor is characterized by rather long parallel connection lengths to the targets of typically some 100 m and up to 1000 m, due to the small magnetic pitch angle (essentially a small local rotational transform) within the magnetic islands [8, 9]. As a consequence, compared to a typical tokamak divertor, cross-field transport becomes increasingly effective compared to parallel transport: while the connection lengths to the divertor near the last closed flux surface (LCFS) are hundreds of meters, "poloidal" distances on an island flux surface are tens of centimeters, and radial distances across island flux surfaces are just a few centimeters. Hence, even small stationary convective cross-field transport levels can have a significant impact on the SOL particle and energy balance [10].

Indications for the role of such transport effects have been observed in W7-X: Multiple diagnostics report non-monotonic temperature [10–13] and density [14, 15] profiles as well as sheared poloidal flows [12, 16, 17] across the SOL islands. The current state-of-the-art mean-field edge transport modeling code for stellarators (EMC3-EIRENE [18, 19]) does not include such convective drift fluxes and generally cannot consistently reproduce the observed plasma profiles across magnetic islands [20, 21].

In addition to the long connection lengths, the island divertor SOL features topological regions that have no counterpart in tokamak divertors [22]: the target shadow regions that stem from the toroidal segmentation of divertor units; and the regions of closed magnetic field lines around the island O-points that exist when not all island flux surfaces are intersected by the divertor. Furthermore, the substructure of the SOL (size and position of the sub-regions, connection length distribution) sensitively depends on external actuators like the island position (which is set by the rotational transform profile) and pitch angle (which can be varied using control

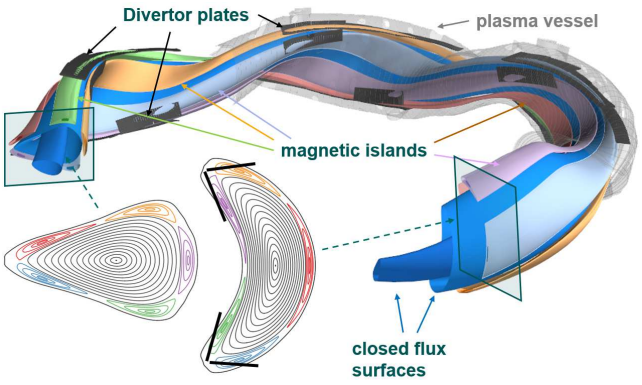

FIG. 1. 3D sketch of W7-X with two closed flux surfaces (blue), the 5/5 magnetic island chain (colored), divertor plates (black), plasma vessel (gray). For clarity, individual components are not shown over the full toroidal extent. Two cross sections are shown as insets.

* see O. Grulke et al. 2024 Nucl. Fusion **64** 112002

coils) [23, 24]. The delicate 3D structure of the island-divertor interaction zone and the observation of poloidal gradients [10, 11] motivates using diagnostics with a large poloidal/radial coverage, over just one line of sight. This work introduces and describes results from a reciprocating Langmuir probe array that aims to maximize the coverage of the island plasma is introduced and utilized. The radial-poloidal distribution of plasma parameters in the island divertor SOL in the magnetic configuration space and across plasma scenarios is explored. Electric fields resulting from electric potential measurements are compared to the direct imaging of drift flows via gas puff imaging. Finally, a survey of 2D resolved probe measurements in the magnetic configuration space of W7-X in the OP2.1 campaign (2022/2023) is given.

II. DIAGNOSTIC SETUP

A. Multi-Purpose Manipulator (MPM) and Gas Puff Imaging (GPI)

As motivated in the introduction, the diagnostic goal is to utilize a reciprocating array of poloidally distributed Langmuir probes with a maximized spatial coverage / resolution. The probe head containing the array is mounted on the Multi-Purpose Manipulator (MPM) [24], which is installed close to the outboard mid-plane and can perform a horizontal fast reciprocation through the SOL, see Fig. 2. The part of the SOL that is accessible by the MPM varies across different magnetic configurations as the number and positions of magnetic islands change [24]. The gas puff imaging (GPI) system [25] is installed in an almost perfectly stellarator-symmetric position to the MPM in the neighboring field period (both diagnostics are at a similar relative toroidal distance of $\approx 15°$ from the so-called *bean* cross section and at a roughly similar poloidal position, roughly resembling the outboard mid-plane of a tokamak. Hence, GPI and MPM are not directly magnetically connected given the range of available rotational transforms in W7-X ($0.8 < \iota_{edge} < 1.25$) [26]. Comparing the fields of view (FoV) in detail, see Fig. 2, the GPI FoV is ≈ 10 cm vertically below the MPM, centering on the island O-point in the *Standard* magnetic configuration [25]. Thus, there is no direct overlap in FoV between the two diagnostics.

B. MPM probe head

The probe head *IPP-FLUC2* depicted in Fig. 2 b) contains 29 Langmuir probe tips that are arranged on a plane that is tangential to the LCFS (averaged across magnetic configurations [24]). The individual cylindrical probes are made of molybdenum with dimensions of $d = h = 2$ mm. The poloidal spacing between poloidally neighboring pins is 4 mm, so that a poloidal base length of

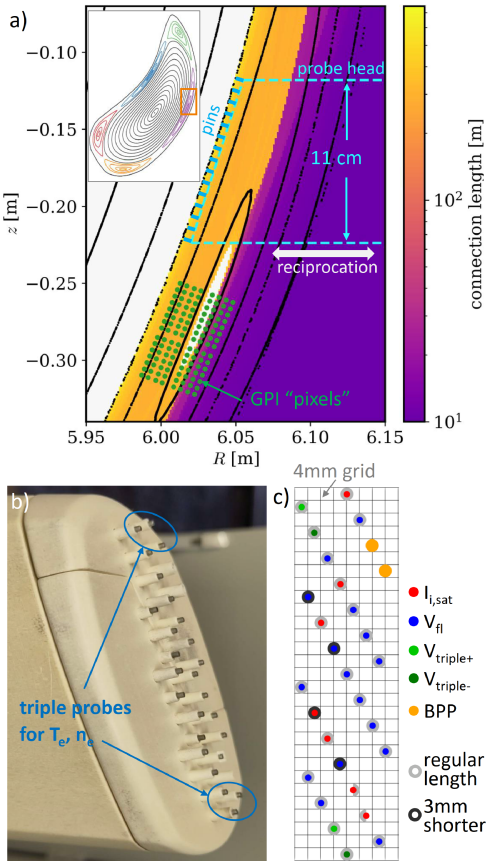

FIG. 2. a) Poincaré representation of the magnetic flux surfaces (black) and color-coded total connection length to divertor targets in the vicinity of the reciprocating probe and gas puff imaging for the magnetic *Standard* configuration. The inset shows the full cross section of W7-X with the region of interest highlighted. Probe outline and GPI pixels are overlaid. b) photograph of the probe head *IPP-FLUC2*. c) map of the 29 electric pins as seen from the plasma.

112 mm is achieved. The pins are arranged such that the interaction via their intrinsic finite plasma perturbation is minimized - each pin has a unique poloidal position (and therefore a separate flux tube), and the pins are spread out toroidally over a distance of 30 mm to maximize separation.

The probe body and sleeves for the pins are made of high purity boron nitride [24]. Using sleeves and electrodes of different lengths, pins can be placed at different radial positions. Typically, most pins are installed on the "top" level (deepest insertion into the plasma), and only a few pins are shorter, placing them radially further out for a given probe head position. The distribution of pin lengths and electric operation modes was varied / optimized over the 2022/2023 W7-X campaign, with the final setup for the magnetic *Standard* configuration experiments in this paper depicted in Fig . 2 c). Most pins are either in floating potential (V_f) mode or constantly negatively biased for ion saturation current ($I_{i,sat}$) mea-

surements. The top three and bottom three pins are used in a triple probe configuration to give T_e, n_e with high time resolution, which has been validated in this geometry against swept probes [13]. In addition, two pins are implemented as ball-pen probes (BPP) [27] and two pins have partially covering boron nitride sleeves to act as a Mach probe. For this work, we focus on the two triple probes and the poloidal array of V_{fl} and $I_{i,sat}$ probes.

C. Constructing 2D maps

The construction of 2D (radial-poidal) V_f maps is illustrated in Fig. 3. From the time traces of individual floating potential measurements, radial profiles are obtained by mapping onto the time trace of the probe position. The probe data, shown in Fig. 3 a), are low-pass filtered to 200 Hz such that fluctuations that are on much faster time scales than the probe movement are averaged out. The resulting time-averaged radial profiles are depicted in Fig. 3 b). Then, data from the 13 V_f probes is arranged to represent the time-averaged V_f distribution in the radial-poloidal cross section as shown in the heat map in Fig. 3 c). For orientation, the four pins shown in a), b) are indicated and a Poincaré plot of the magnetic flux surface geometry is overlaid, with the LCFS position highlighted in magenta. The tilt of the left edge of the V_f data set stems from the shape of the probe, which is designed such that all pins have the same distance from the LCFS.
The similarity of solid vs. dashed profiles for each pin in Fig. 3 b) (reflecting independent measurements during inward vs. outward movement of the probe) supports the robustness of the observation: the same 2D V_f structure is observed in multiple independent measurements.

III. GRADIENTS IN THE ISLAND SOL AND RESULTING DRIFT FLOWS

The example V_f map in Fig. 3 c) already at first glance suggests that the V_f distribution is strongly modified by the magnetic field geometry and exhibits a complex radial and poloidal structure. In this section, the implications of resulting electric fields are discussed.
The V_f map and down-sampled results from the two triple probes of a typical *Standard* configuration measurement (20230323.49 with configuration *EJM007+2520*, ECRH power P_{ECRH}=4.0 MW, at a line-integrated electron density $n_{dl} = 4.0 \cdot 10^{19}\,\mathrm{m}^{-2}$ with path length of ≈1.3 m) are presented in Fig. 4 a). A Poincaré representation of the magnetic flux surfaces is overlaid in black and the LCFS and target shadow region (TSR) boundary are indicated in cyan and purple, respectively. As in Fig. 3, the V_f distribution in between the LCFS and TSR roughly follows the magnetic structure: positive V_f for the innermost island flux surfaces, surrounded by layers of first smaller and then again larger V_f.

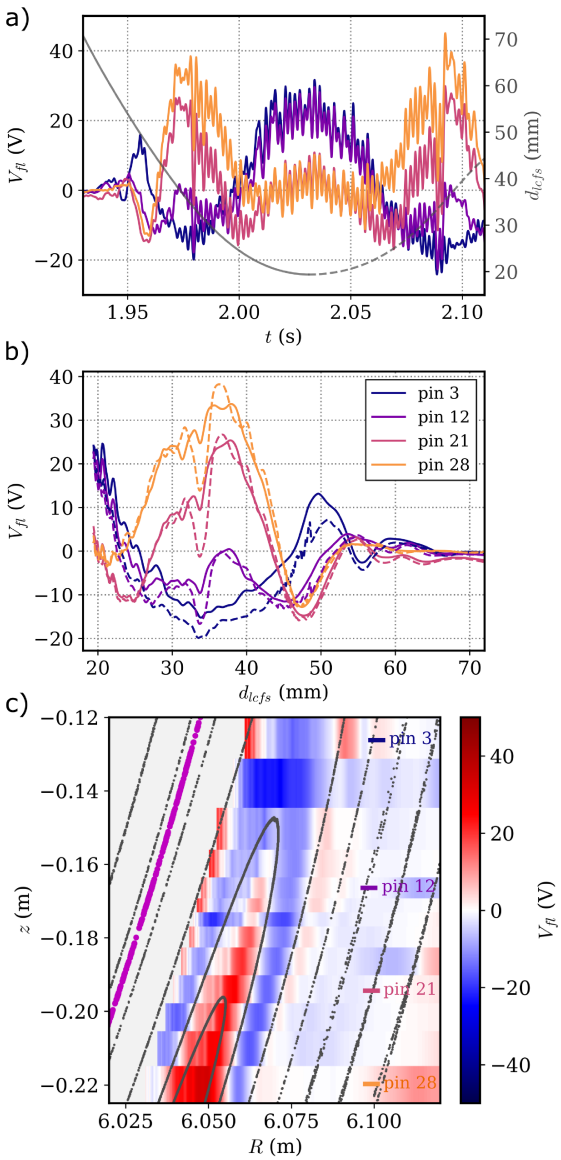

FIG. 3. Construction of radial-poloidal V_f maps for program 20230323.37: a) time traces of four V_f probes (pin number is counted along the probe head from top to bottom) during probe movement (see gray line for probe position), b) low-pass filtered V_f signals mapped to a radial coordinate based on the probe motion (solid lines: inwards movement vs dashed lines: outwards movement of probe), c) a V_f map is assembled from all V_f pins. A Poincaré representation of magnetic flux surfaces is shown by gray dots, and the LCFS is indicated in purple.

The T_e and n_e profiles (circles and diamonds) of the two triple probes are typical for such an experiment: The upper probe shows a clear T_e maximum at the target shadow boundary, in line with multiple previous reports based on MPM Langmuir probe measurements [11, 12, 23, 24, 28, 29]. In stark contrast, the lower triple probe, which is closer to the O-point of the island, does not show any local extrema but rather a broad, flat pro-

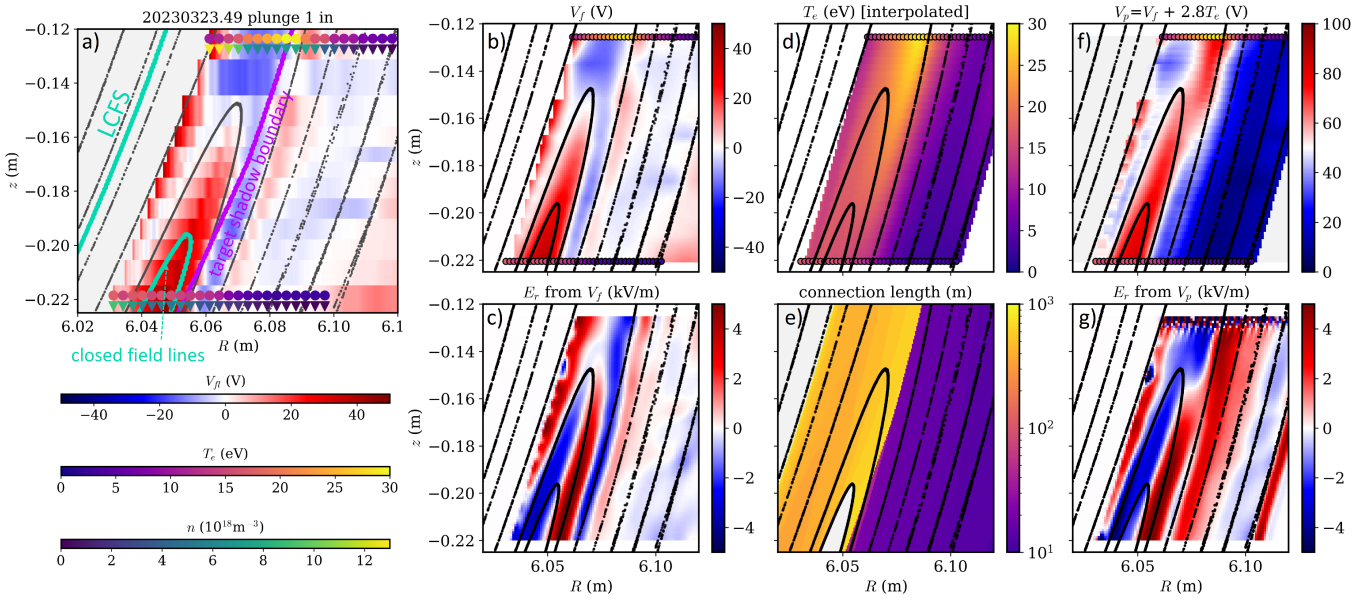

FIG. 4. a) V_f map (constructed as described in Fig. 3) and T_e (circles), n_e (diamonds) profiles at the respective triple probe locations, with magnetic structure overlaid, in *Standard* configuration. b) smoothed V_f map, c) $E_r = -\nabla_r V_f$, d) interpolated T_e map between the two triple profiles, e) connection length reconstruction, f) $V_p = V_f + 2.8T_e$ map, g) $E_r = -\nabla_r V_p$. Poincaré representation is overlaid in all plots. T_e profiles of the two triple probes are overlaid color-coded in b), d), f).

file. Density profiles of both triple probes are also rather shallow in this case.

The V_f structure and T_e gradients imply the existence of time-averaged electric fields. In the simplest approximation, $E_r = -\nabla_r V_f$ is calculated with the radial gradient being along the direction normal to the LCFS. From the (smoothed) V_f map depicted in Fig. 4 b), the E_r approximation in c) is obtained, which features a complex structure of multiple shear layers, with a negative/positive E_r region associated with the central island flux surfaces that has positive V_f. A more rigorous approach towards E_r is to calculate it from the plasma potential via $E_r = -\nabla_r V_p$. However, a 2D resolved V_p measurement is not available. Instead, we estimate $V_p = V_f + 2.8T_e$ [1] using a linear interpolation between the two triple probe T_e profiles to get a pseudo-2D T_e map, see Fig. 4 d). The resulting V_p map depicted in Fig. 4 f) obviously differs from the V_f map, but still shows a localization of plasma parameters by the magnetic islands. The E_r resulting from the V_p estimation (Fig. 4 g)) still features a dominant shear layer in the island center and generally similar E_r magnitudes, but differs in details, particularly in the outer part of the island and upper part of the field of view (the very fine scale features in the upper edge of the field of view are numerical artifacts, though). The linear interpolation of T_e is obviously a drastic simplification, particularly due to the poloidal dependences of V_f shown here, but is the best approach given existing data. In future experiments, more triple probes for a finer T_e resolution will be employed.

The E_r maps in Fig. 4 c), g), imply the existence of sheared poloidal $E_r \times B$ flows. Such flows are observed with GPI, where the time delay estimation from cross-correlating time traces of different pixels as well as 2D (spatial and temporal) Fourier analysis measure the propagation velocity of H_α emission fluctuations [17, 30]. The emission intensity fluctuations are a combination of density and temperature fluctuations that both contribute to a similar degree but cannot easily be untangled [25].

The comparison of poloidal drift velocities evaluated from probe E_r measurements (using the V_p estimation) to poloidal velocities determined by GPI in the same experiment at the same time is presented in Fig. 5. A qualitative agreement between both diagnostics is found: sheared poloidal drift flows of $\sim$km/s are observed by both systems. A more detailed comparison reveals quantitative differences: GPI velocities are typically factor 1.5 to 2 higher than probe velocities. Further, when extrapolating to the undiagnosed space between both systems, a mismatch of the radial position of individual flow channels of ~ 1 cm is found. It is interesting to note that GPI also observes a poloidal structure of the flow patterns, i.e. a dependence on the poloidal position, see the left-most column of views in Fig. 5.

A detailed comparison of the v_{pol} distribution in the island between both diagnostics requires a thorough treatment of e.g. the potentially perturbative nature of both techniques, simplifications in the assumption of plasma potential in the probe data, the use of a rather simple two-point time delay estimation technique for GPI [30], and the possible presence of magnetic field asymmetries between different supposedly symmetric cross-sections of W7-X, and is therefore beyond the scope of this paper.

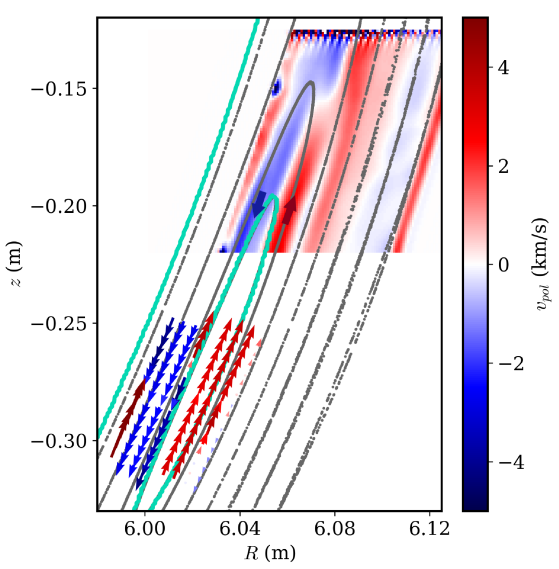

FIG. 5. Poloidal velocities expected by probe E_r measurements (upper part), see Fig. 4, and measured by time delay estimation analysis of GPI (lower part, quiver plot) in *Standard* configuration. The GPI data is mapped from the original location ($\Phi = 274.2°$) to the probe-equivalent cross section at $\Phi = 272.8°$ and displayed in a common cross section with the probe data, assuming stellarator symmetry. Contours of closed field line regions (LCFS and confined region around the O point) are overlaid in cyan.

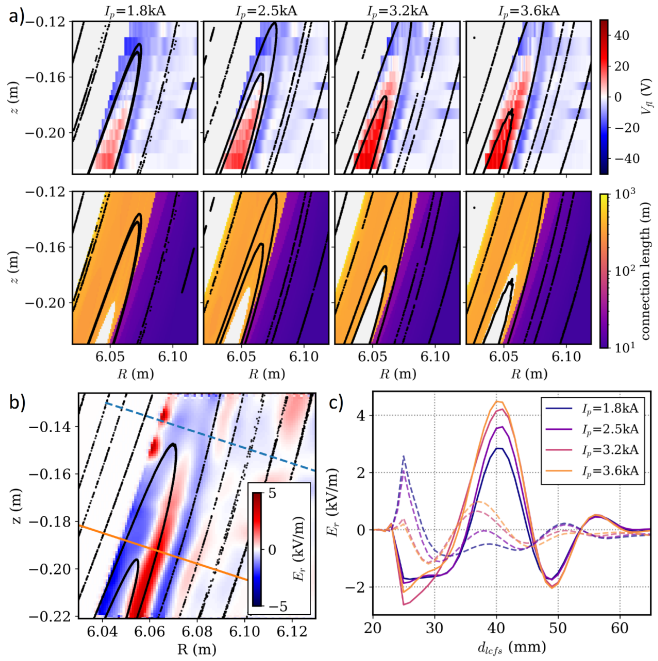

FIG. 6. Role of island position via toroidal plasma current I_p in an experiment with constant heating and density. a) V_f maps and the associated magnetic reconstruction (connection lengths and Poincaré plot) for four probe measurements, b) an example E_r map for the measurement at 1.8 kA. The two highlighted lines are normal to the LCFS and are used to extract 1D E_r profiles. c) Resulting E_r profiles along the two lines in b) during the I_p evolution, with solid and dashed graphs corresponding to the respective solid and dashed line in b).

As in Fig. 4 g), the fine scale features in the uppermost part of the probe data region are a numerical artifact from data processing.

In addition, the V_f / V_p maps in Fig. 4 b), f) also exhibit poloidal gradients, implying the existence of a stationary poloidal electric field of ∼100 V/m. Such a field would cause radial ($v_r = E_{pol} \times B$) flows on the order of 100 m/s, in this case predominantly inwards-directed. Radial flows of such magnitude would be quite relevant to the overall 3D transport balance [10]. However, they are hard to detect in GPI as the very dominant poloidal motion of the fluctuation structures and intrinsic limitations of the GPI viewing geometry [25] make the quantitative evaluation of such a radial motion quite difficult. (Preliminary analysis does not show discernible radial motion of turbulent structures in the GPI FoV in *Standard* configuration.) The comparison of radial flows is therefore deferred to a future investigation.

We finally note that the triple probe profiles, the potential map measurements, and the GPI flow patterns are highly reproducible in similar experiments. However, they are very sensitive to even small changes in the plasma scenario (heating, density, radiation, magnetic configuration including small modification of island size and position), see section IV.

IV. SURVEY ACROSS THE MAGNETIC CONFIGURATION SPACE

After establishing the experimental approach and data analysis technique in the previous sections, this section now discusses trends in the probe data across the magnetic configuration space of W7-X.

A. Radial island movement in *Standard* configuration

The radial position of magnetic islands is defined by the iota profile, where the islands appear at large order rational values - in the case of the W7-X *Standard* configuration at the 5/5 resonance. While the iota profile is set by the magnetic field of the superconducting coils, it can be modified by toroidal currents in the plasma, e.g. the naturally evolving bootstrap currents or externally driven ones [23, 31]. Due to the generally low shear of W7-X (i.e. a rather shallow iota profile), the islands typically move 1-2 mm per kA of plasma current inside the LCFS (assuming the current to be concentrated on the magnetic axis, according to Ampère's law). It was shown

previously that radial island shifts of just $\approx$ 1 cm can have dramatic effects on the SOL transport due to the sensitive interaction with divertor targets [23]. For the magnetic field information shown in the remainder of this paper, the magnetic reconstruction is based on the vacuum magnetic field and the contribution of toroidal current as measured by a continuous Rogowski coil, where the current is assumed to be concentrated on the magnetic axis [23, 31].

The effect of a moderate plasma current evolution on the SOL potential distribution and resulting drift flows is presented in Fig. 6. All data in this figure is from one single 24 s long experiment in *Standard* configuration at constant conditions of P_{ECRH}=3.5 MW, $n_{dl} = 8 \cdot 10^{19}\mathrm{m}^{-2}$, $W_{dia} = 510\,kJ$ (20230323.40). In the course of the discharge, the toroidal (bootstrap) plasma current evolved to almost 4 kA, which is a rather modest value compared to Ref. [23], which featured higher plasma currents due to the lower plasma densities in those experiments. Multiple reciprocating probe measurements were performed throughout the discharge. The V_f maps from four representative probe measurements are shown in Fig. 6 a) along with the magnetic field reconstructions for each respective plasma current. Comparing to the V_f maps in Figs. 3, 4, the existence of a positive V_f region at central island flux surfaces is again observed. However, the positive V_f features at the radially outer side of the island (almost) vanish here, which is typical for situations in higher density plasmas.

Inspecting the plasma current evolution in Fig. 6 a), it becomes obvious that the positive V_f region around the island center increases in size both radially and poloidally for higher plasma currents in the same fashion as the region of closed field lines grows, as corroborated by the magnetic reconstructions where closed field lines are represented as light gray. This relation implies that V_f is at least partly set by sheath conditions. The apparent coincidence of a positive V_f region with a closed field line region agrees with Fig. 4 which is also in *Standard* configuration but disagrees with measurements in other configurations that will be presented later in this section. It is interesting to note that in this higher density experiment, the T_e and n_e profiles (included via the green/blue graphs in Fig. 11) do not react strongly to the plasma current evolution. There is only a small shift of the local peak at $R = 6.09$ m and the "valley" around $R = 6.07$ m in the T_e results of the upper probe. This is in contrast to experiments at smaller density, see Fig. 10 and [23]. Still, the strong similarity of the T_e, n_e profiles in independent measurements in Fig. 11 supports the robustness of the diagnostic technique.

In addition to the positive V_f region increasing in size at higher plasma currents, the V_f magnitude and thus the gradients also react to the I_p evolution. An example $E_r = -\nabla_r V_f$ map is shown for the 1.8 kA measurement in Fig. 6 b). To simplify the E_r data and investigate scalings, we take the E_r profiles along two sections of the E_r map that are normal to the LCFS, i.e. oriented

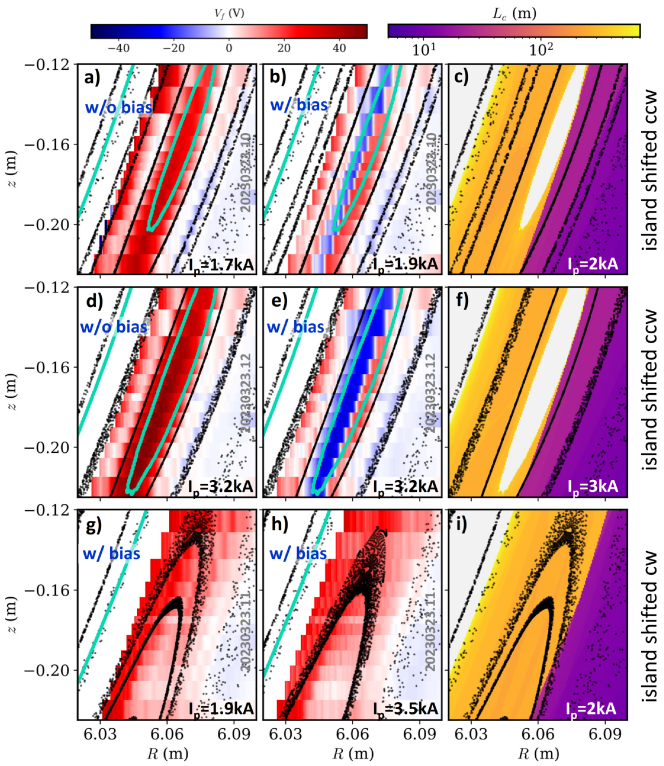

FIG. 7. Maps of V_f (left and middle column) for different experiments on rotated magnetic islands using control coils at a density of $n_{dl} = 4 \cdot 10^{19}\ \mathrm{m}^{-2}$ in *Standard* configuration. Bias voltage to nearby $I_{i,sat}$ pins ($V_{bias} \approx -200V$) was applied in some cases, see inset text. Cyan lines indicate contours of closed field line regions, i.e. the LCFS and around the O point. The right column shows the magnetic reconstruction in terms of connection length and Poincaré representation.

in the *radial* direction. The two section lines are shown as solid blue and dashed orange line, which are arbitrarily chosen to represent two different poloidal positions in the SOL. The resulting E_r profiles for these two lines are presented in Fig. 6 c) for again four measurements at different I_p. For both profiles, E_r increases by ≈ 1.5 kV/m in the main E_r peak region around at a distance from the LCFS of $d_{lcfs} \approx 40$ mm. This observation is in qualitative agreement with a similar scaling of poloidal drift flow velocities with I_p as determined by GPI [17].

B. Poloidal island movement in *Standard* configuration

Using the control coils of W7-X in an asymmetric mode (with different current signs between upper and lower control coils), the magnetic islands can be shifted poloidally by up to $\approx$10 cm when using the maximum current amplitude of 2.5 kA in the control coils [32]. The displacement of magnetic islands is in this case still much smaller than their size. In configurations with both poloidally clockwise (cw) and poloidally counter-

clockwise (ccw) shifted islands, MPM and GPI performed similar measurements to Fig. 5.
In the ccw shifted case, the O-point of the island with a corresponding closed field line region is in the field of view of the MPM probe array, see the reconstructions in the right column of Fig. 7. In this scenario, the V_f maps exhibit unusual behavior in that they depend on the operation mode of the $I_{i,sat}$ pins on the same probe head. If the (negative) bias voltage for $I_{i,sat}$ pins is turned off, an entirely positive V_f map is observed, see the first column in Fig. 7. The V_f distribution is peaked around the center of the island, vertically slightly to the left and below the region of closed field lines (lined out in cyan). However, in the (default) operation mode with negatively biased $I_{i,sat}$ pins operating in addition to the V_f pins, a region of negative floating potential is observed in the center of the island. This region is approximately confined to the radial extent of the closed field line region, although not exactly matching. It does not exhibit any smooth gradients but rather appears as a sharp transition of the V_f measurements of all probe pins, indicating that the island plasma undergoes a transition to a different state. It can be independently reproduced during in- and outward movement of the probe and in different measurements. The spatial extent of the negative V_f region scales with the size of the confined island center region, as corroborated by the top and center rows of Fig. 7, which are taken at different plasma currents and hence slightly different island positions. In the center plot at I_p=3.2 kA, both the regions of closed field lines as well as the region of negative V_f are larger than in the top plot at I_p=1.9 kA. This behaviour is reproducible throughout multiple measurements in this particular island geometry, but it is entirely absent in similar plasmas at different control coil settings for island manipulation. As an example, the situation with the island rotated cw in the bottom row of Fig. 7 does not show any effect of probe bias throughout multiple measurements. In contrast to the unshifted islands in Figs. 3,4, only positive V_f values are observed here, with a radially outwards decaying amplitude of V_f as well as a small poloidal gradient towards higher V_f on the top of the field of view.
A possible explanation for the transiently negative V_f values in the ccw island shifted case is suggested by the coincidence of the negative V_f region with the closed field line region: The island center is a confined toroidal plasma in a closed field line region with a cross section of some cm^2 to some 10 cm^2 and hence a small plasma volume of some 10^{-2}m^3. Inserting multiple negatively biased electrodes ($V_{bias} \approx -200$ V) might impose a negative potential bias in the island center plasma, which is then measured by the V_f pins. Understanding this phenomenon in detail requires future experiments with other diagnostics that might be able to detect any effect on the probe bias on the island plasma - as of now, however, no other sufficiently fast diagnostics exist in locations that are magnetically connected to the MPM probes.
We finally note that the transition to negative V_f values happens on all V_f pins simultaneously, including the shorter probes that measure radially further out of the plasma. This observation implies that the negative V_f phase is not purely due to the probe traversing a certain region of the island - it rather appears that the probe being in a region of closed field lines is a necessary condition, and a second, still unknown actuator is required in addition to cause the V_f flip. This topic of unintentional perturbations caused by electrically biased probes might be related to edge biasing experiments in fusion plasmas, where electrically biased probes are used on purpose to affect shear layers in the plasma edge, e.g. [33, 34]. A deeper analysis is beyond the scope of this paper but might shed light into previous, still unexplained observations of interactions between different Langmuir probe systems in W7-X [35]).

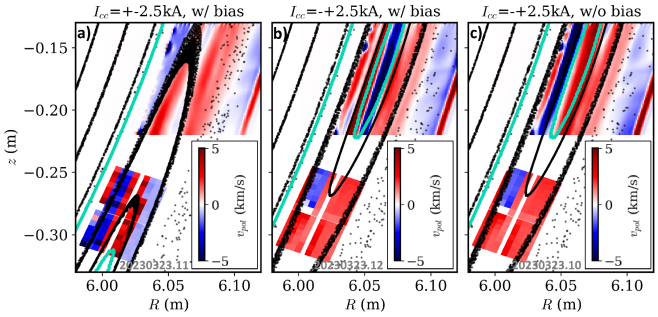

FIG. 8. Poloidal velocity from probes (top) and GPI (bottom) for different island rotation experiments at P_{ECRH}=2 MW, n_{dl}=4e19 m^{-2}, I_p=3 kA in *Standard* configuration. Cyan lines indicate contours of closed field line regions, i.e. LCFS and the island center. a) islands rotated cw, with O point below GPI FoV, b) islands rotated ccw, with O point in MPM FoV and MPM I_{sat} bias on, c) islands rotated ccw, with O point in MPM FoV and MPM I_{sat} bias off.

The v_{pol} maps following from the V_f maps from Fig. 7 have been obtained in similar fashion to Fig. 4 for the case including the T_e contribution for V_p. The results are presented in Fig. 8 along with the flow results determined by GPI [30]. For the cw shifted case in Fig. 8 a), GPI observes three v_{pol} shear layers across the major-radial field of view of just 52 mm, whereas the MPM (closer to the X-point) observes a pattern that is roughly aligned with the island flux surfaces. In this scenario, GPI views the island at approximately the same distance from the O-point as the MPM does in the natural, unshifted configuration.
For the ccw shifted case in Fig. 8 b) and c), GPI observes mostly positive (upwards) v_{pol} except for the upper inner quadrant of the FoV. The MPM v_{pol} results in the ccw shifted scenario depend on the bias of neighboring $I_{i,sat}$ probes, see Fig. 7. Due to the massive effect of the probe bias on V_f measurements in this scenario, the v_{pol} pattern essentially flips between both cases. The "bias off" case, however, seems more reliable as it corresponds to a less perturbative measurement, and in addition agrees better with GPI results in flows around confined plasmas

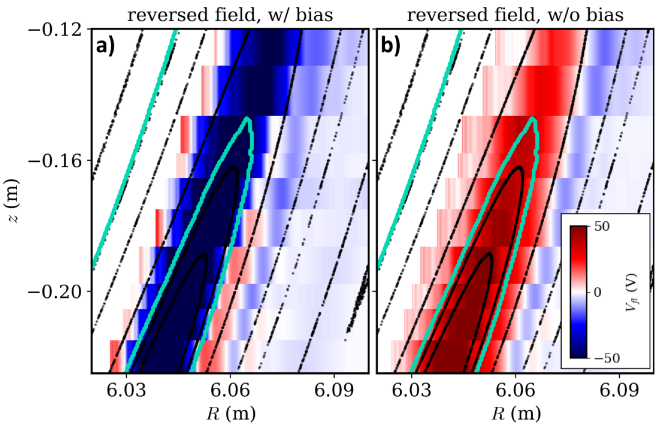

FIG. 9. V_f maps in reversed field *standard* configuration, with a slightly higher iota offset compared to forward field (hence the expected region of closed field lines in cyan is larger than in Fig. 4) for two measurements in program 20230117.67.

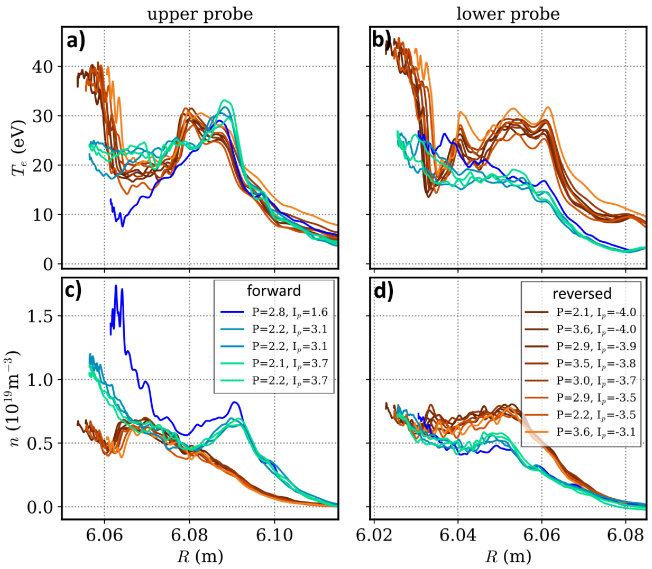

FIG. 10. T_e, n_e profiles at a line integrated density of 4e19m^{-2} in *Standard* configuration for forward (green/blue hues) and reversed (red/orange hues) field direction. The color gradient for each dataset encodes the plasma current, translating to small shifts in radial island position.

center regions, see Fig. 5. Concluding, the flow patterns are found to be complex and fine-structured, and "stitch" the full picture together from GPI and MPM data using different island positions seems beyond the level of confidence in this first set of such experiments.

C. Magnetic field direction

In addition, experiments with reversed magnetic field direction have been conducted. In these experiments, also the magnetic *Standard* configuration was used, but with a slightly higher iota (planar coil iota correction [36] of 500A instead of 250A) and therefore slightly inward shifted islands. Also, a unique error field assessment study was done for these experiments, revealing a different 1/1 error field correction requirement for the trim coils compared to the regular field direction [37].
This discussion of iota and error field correction is relevant, as the experimental results reveal distinct differences between forward and reversed field direction, whereas naively no differences (except for the direction of drifts) would be expected. For the V_f maps presented in Fig. 9, the effect of probe bias of $I_{i,sat}$ pins on the V_f measurements is once more displayed. In a series of more than 30 measurements, it was consistently observed that in situations with active bias voltage a negative V_f is seen in the island center, where as positive V_f is seen in experiments without bias voltage on the $I_{i,sat}$ pins. This behavior is similar to the case of the ccw shifted island in forward field direction (see Fig. 7), but is entirely absent in regular (unshifted islands) forward configuration, as well as other magnetic configurations. We are therefore confident that it is not a measurement error but a true physics observation. As this peculiar bias effect on V_f might be related to the probe being in a large region of closed field lines (see ccw shifted case in Fig. 7 and the discussion in section IV.B), the frequent observation of this effect in reversed field might imply that the region of closed field lines in the reversed field configuration might be larger than expected from the reconstruction (see cyan line in Fig. 9).
As a further indication for unusual behavior upon field reversal, we note that in the reversed field experiments GPI observed apparently random flips of the SOL flow pattern in some measurements, where the poloidal flow directions clearly flip, unrelated to MPM operation and also for no other obvious reason. This observation suggests that the island flow patterns might bifurcate between two local equilibria. However, GPI does not see direct evidence of different size or position of the island confined region in reversed field, in it's own magnetic island (which is separate from the island probed by the MPM).
The effect of the bias-induced V_f drop in the island center as well as the general effect of field reversal is further showcased in the T_e, n_e profiles in Figs. 10, 11. For the lower density measurements in Fig. 10, there is a consistent profile shape for each field direction, with smaller differences in each dataset that can well be assigned to the island position via plasma current, see color scale. The clear difference between the "average forward field" and "average reversed field" profile shape can be caused by both drift effects (which reverse with B) and different field asymmetries due to resonant error fields. As an example, the location of the T_e peak at the upper probe around 6.08 m to 6.09 m depends on the field direction, although the location of the target shadow boundary (see Fig. 4 a)) is not expected to depend on field direction. Further, higher densities are observed in forward field at

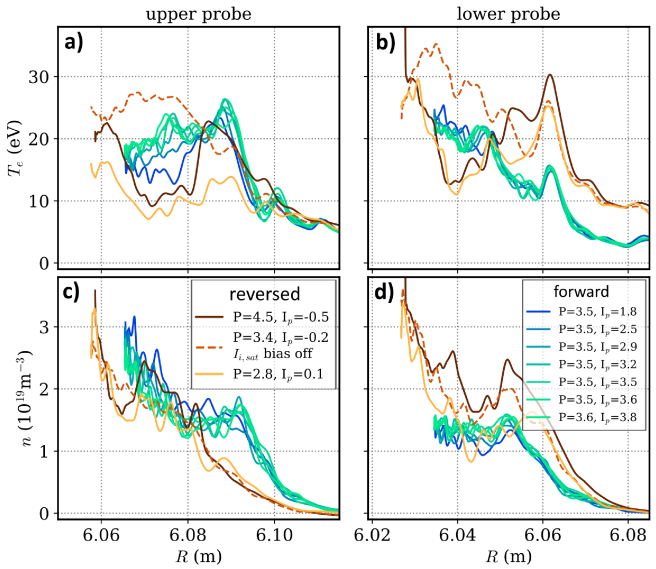

FIG. 11. T_e, n_e profiles at a line integrated density of 8e19m^{-2} in *Standard* configuration for forward (green/blue hues) and reversed (red/orange hues) field direction. The color gradient for each dataset encodes the plasma current.

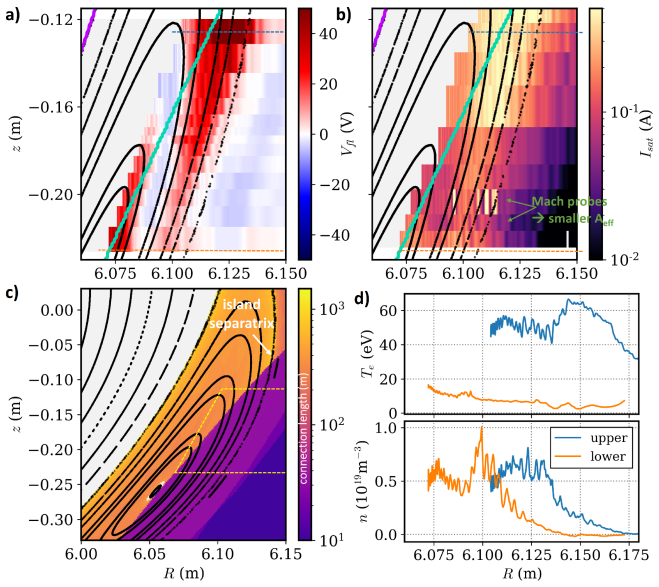

FIG. 12. Probe results in the *Low shear* configuration for program 20230307.54. a)V_f map, b) $I_{i,sat}$ map, both overlaid with Poincaré map and LCFS (magenta) and target shadow boundary (cyan), c) magnetic reconstruction in a larger FoV, with regions of probe data lined out by yellow dashed lines, d) T_e, n_e profiles along the blue and orange dashed lines given in a) and b).

the upper probe and in reversed field at the lower probe, hinting at the effect of drift flows.

At higher densities in Fig. 11, the forward field profiles retain the shape from Fig. 10, just at lower temperature and higher density. The effect of the plasma current evolution is small but still visible (particularly in the upper probe) by the ordering of profiles by color gradient. The reversed field data set includes a situation (dashed line) where the bias voltage of $I_{i,sat}$ probes was turned off and an effect on the V_f was seen, see Fig. 9. In this measurement, the T_e valley in the center of the island vanishes, while n_e is rather unaffected. This observation implies that in the reversed field case, the profile measurement without $I_{i,sat}$ bias are more likely to be the "true" profiles. We note that this behavior was observed independently on several occasions, unrelated to external parameters like heating power or plasma current, with always the same phenomenology. It only occurred in reversed field *standard* configuration and in forward *standard* configuration with ccw shifted islands (see Fig. 7) - in all other magnetic configurations the presence of bias voltage does not affect the results of other probes. Therefore, a technical malfunction is highly unlikely.

We finally need to emphasize that the T_e measurements with triple probes inherently assume a Maxwellian energy distribution. While triple probes have been successfully benchmarked against classic swept probes in [13], those experiments did not include closed field line regions in the island center. The effects discussed in this section call for measurements of the electron energy distribution in closed field line regions of magnetic islands in future campaigns of W7-X.

D. *Low shear* configuration

The "low shear, outward shifted" configuration (*MMG000+2520*) presented in Fig. 12 features particularly large 5/5 magnetic islands. In this experiment, the island size is further increased using the control coils in a symmetric mode with $Icc = +1.5$ kA in all 10 control coils. The V_f map in Fig. 12 exhibits a strong modulation of V_f with the magnetic structure. In comparison to the previous example, island flux surfaces appear to have an even stronger impact than the connection length on the V_f distribution, as the TSR boundary (overlaid in cyan) is not reflected by any features in the V_f data. Instead, a band of positive V_f exists along the outer flux surfaces of the island, with a V_f peak towards the upper part of the probe FoV (i.e. towards the X-point). In addition, the more central island flux surfaces exhibit a V_f peak towards the O-point, while a roughly flux surface-aligned band of negative V_f separates the two positive V_f regions. In a crucial difference to Fig. 4 a), the region of positive V_f around the island O-point does *not* correspond a region of closed field lines in this magnetic configuration.

The gradients of this V_f map implies both a sheared E_r profile (similar to Fig. 4 but with a different pattern) and a considerable E_{pol} with magnitudes of up to 1 kV/m, suggesting radial velocities of several 100 m/s. A comparison to GPI is unfortunately not possible as the GPI FoV does not cover the SOL for this rather outward shifted

magnetic configuration.
Further, the map of $I_{i,sat}$ currents in Fig. 12 b) reveals a similar tendency, in the form of an $I_{i,sat}$ peak towards the upper part of the FoV along the outer island flux surfaces. The T_e, n_e profiles of the two triple probes exhibit very different T_e profiles but approximately similar n_e profiles. Hence, the higher $I_{i,sat}$ towards the upper part of the FoV can be attributed predominantly to the temperature contribution ($I_{i,sat} \sim n_e\sqrt{T_e}$). Upon closer inspection, the density profile at the lower triple probe features a maximum at the island separatrix as well as at the innermost measurement points, indicating the role of transport along island flux surfaces. However, it is puzzling that the T_e profiles show such a remarkable poloidal gradient across a spatial scale of 10 cm, which is much smaller than the island size. We note that the highly reproducible nature of this result after multiple measurements gives high confidence in the validity of the measurement. Further, the same probe operated in other magnetic configurations on the same experiment day and yielded more symmetric T_e profiles, further corroborating that the poloidal asymmetry in Fig. 12 is true. It could be conjectured that the higher T_e (and V_f) towards the upper part of the FoV is a consequence of the island separatrix (the outermost flux surface shown in Fig. 12) intersecting the TSR at $z = -0.07$ m, (i.e. a few cm above the probe FoV, as indicated by the white arrow in Fig. 12 c)), where higher T_e might be expected due to the magnetically close proximity to the LCFS and the long connection lengths of up to 1000 m which imply that parallel losses to the divertor are small there.

E. *High Mirror* configuration

The *High Mirror* configuration (*KKM000+2520*) also features a 5/5 island chain building an island divertor configuration. In contrast to the *Standard* configuration, the islands have a different interaction zone with the divertor targets, resulting in a slightly different connection length distribution in the SOL with a smaller (or absent) closed field line region at the O-points and a radially narrower region of long connection lengths, see Fig. 13 b). A set of probe measurements in this configuration is presented in Fig. 13 a) and c). The T_e, n_e profiles of the triple probe reveal a clear T_e peak around the target shadow boundary at R=6.07 m, as well as a n_e peak a few mm further out. The T_e profiles are quite similar across the data set whereas the n_e profiles show a stronger dependence on the plasma operation conditions - in particular, higher densities and a stronger density peaking is observed for experiments at higher heating power and line integrated density. The double lines per color represent the inward and outward movement of the probe, supporting the robustness of the measurements. For technical reasons, the lower triple probe was unavailable for these experiments.
The V_f maps in 13 c) reveal a somewhat different structure compared to *Standard* configuration. For lower heating powers and densities, mostly positive V_f is observed, with a local maximum in the "intermediate" connection length region (purple in Fig. 13 b)). Notably, a small region of negative V_f around (R=6.03 m, z=-0.2 m) is consistently seen in all such measurements, currently lacking an explanation. Towards higher powers and densities, the V_f maps transforms such that there appear to be two distinct bands of positive V_f in the probe FoV: tied to the central island flux surfaces for the lower part of the FoV, and along the target shadow boundary for the upper part for the FoV. As shown by the bottom subplots in Fig. 13 c), the E_r map and hence the expected drift flows change accordingly. Unfortunately, the GPI FoV does not capture the relevant part of the SOL in this magnetic configuration, hence no flow maps for this region are available.

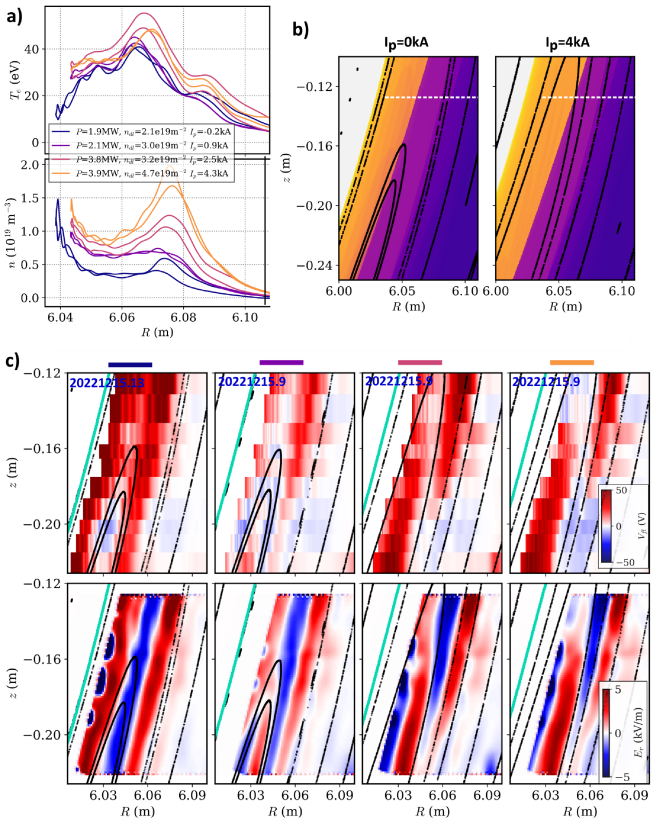

FIG. 13. Probe results in the *High Mirror* configuration:
a) T_e, n_e profiles for four different measurements of the upper triple probe. Double lines per color represent the in- and outward movement of the probe.
b) reconstruction of connection lengths and Poincaré representation at plasma currents of I_p=0 kA and I_p=4 kA. White dashed lines indicate the position where T_e, n_e are taken. Colormap is identical to the colorbar in Fig. 12 c).
c) V_f (top) and $E_r = -\nabla_r V_f$ (bottom) maps corresponding to the profiles in a), see the line color for reference.

F. *Low Iota* configuration

In contrast to the previous magnetic configurations, the *Low Iota* configuration features a 5/6 magnetic island chain at the LCFS. In this configuration, an X-point is located just below the probe FoV, such that the probe measures in the private flux region (PFR) outside the island, just above the X-point [38]. The V_f maps in Fig. 14 reveal a poloidally uniform, positive V_f distribution in cases of high heating power densities, see the left subplots. Two flux-surface aligned bands of positive E_r are observed. Towards lower power densities, a fine structure emerges: in the center subplots, a poloidal variation of V_f and E_r appears. For the lowest power density in the right subplots, only a small band of positive V_f (and hence E_r) remains in place. It is entirely unexpected that such features exist deep in the PFR, about 4 cm radially away from the islands. We note that all examples shown here are well reproduced in many individual measurement and currently still lack explanation.

It is interesting to note that a strongly localized asymmetric radiation feature was observed experimentally in *Low iota* configuration in a part of the PFR that is magnetically connected to the MPM [9]. It could be conjectured that this strongly localized radiation feature relates to the V_f distribution in Fig. 14. Relatedly, EMC3-EIRENE simulations in *Low iota* configuration also revealed localized small-scale radiation features in the islands, though not in the PFR [9].

Further, the low iota configuration is particularly susceptible to plasma beta effects [39]. The dependence of the probe results on heating power and global densities, comparing the three measurements in Fig. 14, might suggest the role of beta effects on the magnetic topology (plasma current effects on island position were not observed to be relevant in this configuration).

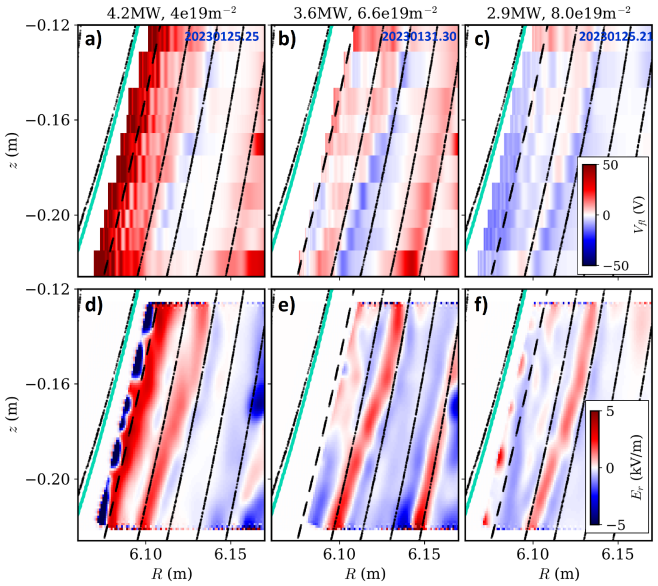

FIG. 14. V_f (top) and $E_r = -\nabla_r V_f$ (bottom) maps in the *Low Iota* configuration. Here, the cyan contour represents the outer island separatrix, indicating that all probe measurements are located in the private flux region.

V. SUMMARY AND CONCLUSION

Reciprocating Langmuir probe arrays uncover a complex structure of plasma parameters in the island divertor SOL in the Wendelstein 7-X stellarator. Electron temperature and density as well as floating potential reveal substantial poloidal gradients as well as a radially non-monotonous profile shape. Distinct features in the plasma parameter distributions are related to the unique magnetic structure of the island divertor SOL, i.e. the presence of a closed field line region around the island O-point and the presence of a "target shadow boundary", which manifests as large radial gradient in connection length. Typical scale lengths of features in the plasma parameters are on the order of cm, i.e. much smaller than the island size. Hence, plasma parameters appear to be entangled with the local magnetic characteristics in a non-trivial way, so that further understanding requires both a broader experimental database and improved magnetic reconstruction capabilities, as no clear picture on the relation of experimental results to magnetic features emerges. Both the island flux surfaces (see the flux surface aligned V_f structures in island center) and the connection length to the target (see the T_e peak at the target shadow boundary) appear to play a decisive role for the SOL plasma. For future investigation, disentangling the role of connection length along vs against the magnetic field could shed further light onto the role of sheath physics for electric potential measurements, as in this work only the total (target-to-target) connection length was presented in the magnetic reconstruction figures. For the long connection length regions (or confined island center), one could conjecture that particles might be trapped (either in the main field "mirror", or in the coil ripple), such that neoclassical transport effects become relevant. In addition, it is observed that in the closed field line region of the island center, biased Langmuir probes can impose a different plasma potential onto this small private plasma region, where the probe itself can act as a limiter. This phenomenon is on the one hand an unintended confounder, but on the other hand opens up a tool to diagnose the existence of the closed field line region.

The 2D potential structures in the island divertor SOL imply the existence of electric fields and therefore ExB drift flows, which are mostly directed in the poloidal direction with magnitudes of ~km/s and can exhibit multiple shear layers. Using gas puff imaging, such flows are observed in qualitative agreement with the flows expected from the probe potential measurements. Typical structure sizes of the flow patterns can be as small as 1 cm, i.e. much smaller than the magnetic islands. These

flows are a significant contribution perpendicular transport in the SOL, as the pitch angle in the island divertor in W7-X can be as low as $\Theta = 10^{-3}$, which strongly amplifies the impact of poloidal drift flows compared to parallel heat transport [8]. For typical SOL plasma conditions at low to medium densities, this transport channel would dominate all others by at least an order of magnitude [10]. This is a challenge for mean field transport models in stellarators, which to date do not include such flows [20]

The detailed understanding of the behavior of these flow patterns in the magnetic configuration space of W7-X requires a better understanding of the magnetic field structure. Quantitative differences between GPI and MPM measurements might be due to residual field errors that cause asymmetries between different magnetic islands. Further, the experimental indications in the closed field line region (based on floating potential measurements) suggest that the plasma-divertor interaction might not fit the simple assumptions - as an example, the region of closed field lines appears to be larger than expected in the reversed magnetic field direction, which might again be due to resonant field errors.

Magnetic configurations beyond the *Standard* configuration are briefly touched in this work, and reveal a wide diversity of SOL structures that motivate future experiments and investigations.

VI. ACKNOWLEDGMENTS

The authors thank Victoria Winters, IPP Greifswald, for support in the conduction of key experiments.
This work has been carried out within the framework of the EUROfusion Consortium, funded by the European Union via the Euratom Research and Training Programme (Grant Agreement No 101052200 — EUROfusion). Views and opinions expressed are however those of the author(s) only and do not necessarily reflect those of the European Union or the European Commission. Neither the European Union nor the European Commission can be held responsible for them.
Support for MIT participation was provided by the US Department of Energy, Fusion Energy Sciences, Award DE-SC0014251.

[1] P. C. Stangeby, *The Plasma Boundary of Magnetic Fusion Devices* (CRC Press, 2000).
[2] D. Carralero, M. Siccinio, M. Komm, S. Artene, F. D'Isa, J. Adamek, L. Aho-Mantila, G. Birkenmeier, M. Brix, G. Fuchert, M. Groth, T. Lunt, P. Manz, J. Madsen, S. Marsen, H. Müller, U. Stroth, H. Sun, N. Vianello, M. Wischmeier, and E. Wolfrum, Nuclear Fusion **57**, 056044 (2017).
[3] O. Garcia, R. Pitts, J. Horacek, A. Nielsen, W. Fundamenski, J. Graves, V. Naulin, and J. J. Rasmussen, Journal of Nuclear Materials **363-365**, 575 (2007).
[4] P. Manz, C. Hufnagel, A. Zito, D. Carralero, M. Griener, T. Lunt, O. Pan, M. Passoni, B. Tal, M. Wischmeier, and E. Wolfrum, Physics of Plasmas **27**, 022506 (2020), https://doi.org/10.1063/1.5133839.
[5] R. König, P. Grigull, K. McCormick, Y. Feng, J. Kisslinger, A. Komori, S. Masuzaki, K. Matsuoka, T. Obiki, N. Ohyabu, H. Renner, F. Sardei, F. Wagner, and A. Werner, Plasma Physics and Controlled Fusion **44**, 2365 (2002).
[6] Y. Feng *et al.*, Nuclear Fusion **46**, 807 (2006).
[7] T. S. P. et al., Nuclear Fusion **62**, 042022 (2022).
[8] Y. Feng, M. Kobayashi, T. Lunt, and D. Reiter, Plasma Physics and Controlled Fusion **53**, 024009 (2011).
[9] V. R. Winters, F. Reimold, Y. Feng, D. Zhang, V. Perseo, E. R. Flom, F. Henke, D. M. Kriete, N. Maaziz, G. Partesotti, M. Jakubowski, R. König, M. Krychowiak, and the W7-X Team, "First experimental confirmation of island sol geometry effects on detachment in wendelstein 7-x," (2024), submitted to NF.
[10] E. Flom, M. Kriete, M. Krychowiak, N. Maaziz, V. Perseo, F. Reimold, O. Schmitz, V. Winters, S. Baek, S. Ballinger, C. Killer, F. Henke, D. Gradic, R. König, A. von Stechow, J. Terry, and W.-X. Team, "Observation of a drift-driven transport regime in the island divertor of wendelstein 7-x," (2024), https://arxiv.org/abs/2312.01240.
[11] T. Barbui, M. Krychowiak, O. Schmitz, S. Bozhenkov, E. Flom, G. Fuchert, C. Killer, R. König, M. Jakubowski, J. M. Burgos, E. Pasch, E. Scott, and W.-X. Team, Nuclear Fusion **60**, 106014 (2020).
[12] C. Killer, O. Grulke, P. Drews, Y. Gao, M. Jakubowski, A. Knieps, D. Nicolai, H. Niemann, A. P. Sitjes, G. Satheeswaran, and W.-X. Team, Nuclear Fusion **59**, 086013 (2019).
[13] C. Killer, Y. Narbutt, O. Grulke, and the W7-X Team, Nuclear Fusion **61**, 096038 (2021).
[14] S. Zoletnik, G. Anda, C. Biedermann, A. D. Carralero, G. Cseh, D. Dunai, C. Killer, G. Kocsis, A. Krämer-Flecken, M. Otte, B. Shanahan, T. Szepesi, M. Vecsei, L. Zsuga, and W.-X. Team, Plasma Physics and Controlled Fusion **62**, 014017 (2019).
[15] B. Csillag, S. Zoletnik, C. Killer, M. Vecsei, G. Anda, D. Dunai, S. Hegedus, D. Refy, D. Nagy, M. Otte, and the W7-X Team, Nuclear Fusion **64**, 016017 (2023).
[16] A. Kraemer-Flecken, X. Han, T. Windisch, J. Cosfeld, P. Drews, G. Fuchert, J. Geiger, O. Grulke, C. Killer, A. Knieps, Y. Liang, S. Liu, and M. Rack, Plasma Physics and Controlled Fusion **61**, 054003 (2019).
[17] S. Ballinger, S. Baek, A. von Stechow, J. Terry, C. Killer, and W.-X. Team, "Sheared flows in the scrape-off layer of the w7-x stellarator," (2024), manuscript in preparation.
[18] Y. Feng, F. Sardei, and J. Kisslinger, Journal of Nuclear Materials **266-269**, 812 (1999).
[19] Y. Feng, H. Frerichs, M. Kobayashi, A. Bader, F. Effenberg, D. Harting, H. Hoelbe, J. Huang, G. Kawamura, J. D. Lore, T. Lunt, D. Reiter, O. Schmitz, and D. Sharma, Contributions to Plasma Physics **54**, 426

(2014).
[20] D. Bold, F. Reimold, H. Niemann, Y. Gao, M. Jakubowski, C. Killer, V. R. Winters, and the W7-X Team, Nuclear Fusion **62**, 106011 (2022).
[21] D. Bold, F. Reimold, Y. Gao, M. Jakubowski, C. Killer, and V. Winters, "Impact of transport models on local measurements in w7-x using synthetic diagnostics with emc3-eirene and comparison to experimental observations in the w7-x island scrape-off layer," (2024), manuscript in preparation.
[22] K. C. Hammond, Y. Gao, M. Jakubowski, C. Killer, H. Niemann, L. Rudischhauser, A. Ali, T. Andreeva, B. D. Blackwell, K. J. Brunner, B. Cannas, P. Drewelow, P. Drews, M. Endler, Y. Feng, J. Geiger, O. Grulke, J. Knauer, S. Klose, S. Lazerson, M. Otte, F. Pisano, U. Neuner, A. P. Sitjes, K. Rahbarnia, J. Schilling, H. Thomsen, and G. A. W. and, Plasma Physics and Controlled Fusion **61**, 125001 (2019).
[23] C. Killer, Y. Gao, V. Perseo, L. Rudischhauser, K. Hammond, B. Buttenschön, T. Barbui, B. D. Blackwell, K.-J. Brunner, P. Drews, M. Endler, J. Geiger, O. Grulke, M. Jakubowski, S. Klose, J. Knauer, A. Knieps, R. König, Y. Li, U. Neuner, H. Niemann, M. Otte, J. Schilling, A. P. Sitjes, K. Rahbarnia, T. Stange, and W.-X. Team, Plasma Physics and Controlled Fusion **61**, 125014 (2019).
[24] C. Killer, P. Drews, O. Grulke, A. Knieps, D. Nicolai, G. Satheeswaran, and on behalf of the W7-X Team, Journal of Instrumentation **17**, P03018 (2022).
[25] J. Terry, A. von Stechow, S. Baek, S. Ballinger, O. Grulke, C. von Sehren, R. Laube, C. Killer, F. Scharmer, K. Brunner, and W.-X. team, "The realization of a gas puff imaging system on the wendelstein 7-x stellarator," (2024), submitted to Rev. Sci. Instrum.
[26] J. Geiger, R. C. Wolf, C. Beidler, A. Cardella, E. Chlechowitz, V. Erckmann, G. Gantenbein, D. Hathiramani, M. Hirsch, W. Kasparek, J. Kißlinger, R. König, P. Kornejew, H. P. Laqua, C. Lechte, J. Lore, A. Lumsdaine, H. Maaßberg, N. B. Marushchenko, G. Michel, M. Otte, A. Peacock, T. S. Pedersen, M. Thumm, Y. Turkin, A. Werner, and D. Z. and, Plasma Physics and Controlled Fusion **55**, 014006 (2012).
[27] J. Adámek, J. Stöckel, M. Hron, J. Ryszawy, M. Tichý, R. Schrittwieser, C. Ionită, P. Balan, E. Martines, and G. V. Oost, Czechoslovak Journal of Physics **54**, C95 (2004).
[28] P. Drews, C. Killer, J. Cosfeld, A. Knieps, S. Brezinsek, M. Jakubowski, C. Brandt, S. Bozhenkov, A. Dinklage, J. Cai, M. Endler, K. Hammond, M. Henkel, Y. Gao, J. Geiger, O. Grulke, D. Höschen, R. König, A. Krämer-Flecken, Y. Liang, Y. Li, S. Liu, H. Niemann, D. Nicolai, O. Neubauer, U. Neuner, M. Rack, K. Rahbarnia, L. Rudischhauser, N. Sandri, G. Satheeswaran, S. Schilling, H. Thomsen, T. Windisch, and S. Sereda, Nuclear Materials and Energy **19**, 179 (2019).
[29] S. C. Liu, Y. Liang, H. Q. Wang, C. Killer, P. Drews, A. Knieps, X. Han, O. Grulke, A. Krämer-Flecken, G. S. Xu, N. Yan, D. Höschen, D. Nicolai, G. Satheeswaran, J. Geiger, M. Henkel, Z. Huang, R. König, Y. Li, O. Neubauer, K. Rahbarnia, N. Sandri, B. Schweer, E. H. Wang, Y. M. Wang, S. Xu, and X. Gao, Physics of Plasmas **27**, 122504 (2020), https://doi.org/10.1063/5.0016151.
[30] S. Baek, S. Ballinger, O. Grulke, C. Killer, A. von Stechow, J. Terry, and W.-X. Team, "Gas puff imaging of plasma turbulence in the magnetic island scrape-off layer of w7-x," (2024), submitted to NME.
[31] Y. Gao, J. Geiger, M. W. Jakubowski, P. Drewelow, M. Endler, K. Rahbarnia, S. Bozhenkov, M. Otte, Y. Suzuki, Y. Feng, H. Niemann, F. Pisano, A. Ali, A. P. Sitjes, M. Zanini, H. Laqua, T. Stange, S. Marsen, T. Szepesi, D. Zhang, C. Killer, K. Hammond, S. Lazerson, B. Cannas, H. Thomsen, T. Andreeva, U. Neuner, J. Schilling, A. Knieps, M. Rack, and Y. L. and, Nuclear Fusion **59**, 106015 (2019).
[32] H. Renner, J. Boscary, V. Erckmann, H. Greuner, H. Grote, J. Sapper, E. Speth, F. Wesner, M. Wanner, and W.-X. Team, Nuclear Fusion **40**, 1083 (2000).
[33] R. J. Taylor, M. L. Brown, B. D. Fried, H. Grote, J. R. Liberati, G. J. Morales, P. Pribyl, D. Darrow, and M. Ono, Phys. Rev. Lett. **63**, 2365 (1989).
[34] G. Grenfell, B. van Milligen, U. Losada, W. Ting, B. Liu, C. Silva, M. Spolaore, and C. H. and, Nuclear Fusion **59**, 016018 (2018).
[35] C. Killer, O. Grulke, M. Endler, and L. Rudischhauser, in *Proceedings of the 48th EPS Conference on Plasma Physics* (2022).
[36] S. A. Lazerson, Y. Gao, K. Hammond, C. Killer, G. Schlisio, M. Otte, C. Biedermann, M. Spolaore, S. Bozhenkov, J. Geiger, O. Grulke, D. Nicolai, G. Satheeswaran, H. Niemann, M. Jakubowski, P. Drewelow, A. P. Sitjes, A. Ali, B. Cannas, F. Pisano, R. König, G. Wurden, G. Kocsis, T. Szepesi, U. Wenzel, M. Mulsow, K. Rahbarnia, J. Schilling, U. Neuner, T. Andreeva, H. Thomsen, J. Knauer, K. J. Brunner, B. Blackwell, M. Endler, S. Klose, and L. R. and, Nuclear Fusion **59**, 126004 (2019).
[37] S. A. Lazerson, M. Otte, M. Jakubowski, B. Israeli, G. A. Wurden, U. Wenzel, T. Andreeva, S. Bozhenkov, C. Biedermann, G. Kocsis, T. Szepesi, J. Geiger, T. S. Pedersen, D. Gates, and T. W.-X. Team, Nuclear Fusion **57**, 046026 (2017).
[38] C. Killer, B. Shanahan, O. Grulke, M. Endler, K. Hammond, L. Rudischhauser, and W.-X. Team, Plasma Physics and Controlled Fusion **62**, 085003 (2020).
[39] A. Knieps, Y. Suzuki, J. Geiger, A. Dinklage, S. Zhou, K. Rahbarnia, J. Schilling, U. Neuner, H. Thomsen, M. Jakubowski, R. Koenig, M. Endler, Y. Gao, A. Sitjes, H. Niemann, M. Beurskens, S. Bozhenkov, Y. Liang, and the W7-X Team, Nuclear Fusion **62**, 026011 (2021).